

Experimental detection of vortices in magic-angle graphene

Received: 5 February 2025

Accepted: 6 October 2025

Published online: 21 November 2025

 Check for updates

Marta Perego¹✉, Clara Galante Agero¹, Alexandra Mestre Torà¹,
Elías Portolés¹, Artem O. Denisov¹, Takashi Taniguchi², Kenji Watanabe³,
Filippo Gaggioli^{4,5}, Vadim Geshkenbein⁴, Gianni Blatter^{4,6},
Thomas Ihn^{1,6} & Klaus Ensslin^{1,6}

Superconducting magic-angle twisted-layer graphene (MATLG) is a promising candidate for superconducting electronics due to its electrical tunability. While the microscopic origins of superconductivity in MATLG have been intensively studied, many aspects of its phenomenology remain unexplored due to the challenges associated with studying two-dimensional (2D) materials. Here, we report the first direct experimental evidence of superconducting vortices in MATLG, a hallmark of type-II superconductors. Field-dependent critical current measurements in a gate-tuned Josephson junction reveal Fraunhofer-like patterns characteristic of ultrathin films with weak transverse screening. These patterns exhibit sudden shifts attributed to spontaneous vortex penetration into the leads. With the leads at the edge of the superconducting dome, we observe bistable V - I fluctuations linked to rapid vortex dynamics. Time-dependent measurements provide the vortex energy scale, the London penetration depth, and superfluid stiffness, consistent with recent kinetic inductance studies. These findings establish gate-defined Josephson junctions as versatile sensors of vortex dynamics in 2D superconductors.

Twisted-layer graphene has emerged as a new platform for realizing non-trivial correlated states^{1–3}, with superconducting bi- and multilayer systems attracting particular interest recently^{4–8}. Superconductivity in these two-dimensional (2D) structures can be electrically tuned, enabling the implementation of gate-defined devices. Much research has focused on magic-angle twisted bilayer graphene (MATBG), which has become a versatile platform for superconducting electronics^{9–14}. Recently, alternating-twist magic-angle multilayer graphene structures have emerged as a novel family of moiré superconductors^{8,15–18}; in this configuration, each successive layer is rotated by an angle of $\pm \theta$ relative to the previous one, following an alternating sequence. Superconductivity in these multilayer structures is characterized by higher critical currents, critical magnetic fields, and critical temperatures than in MATBG. Moreover, their band structure can be tuned by a

transverse electrical field, the so-called displacement field¹⁹, providing additional versatility for device operation. As a result, alternating-twist magic-angle multilayer graphene structures are promising candidates for future superconducting electronic devices.

Here, we implement a gate-defined Josephson junction (JJ) in four-layer twisted graphene (MAT4G), see ref. 20 for a similar setup in a trilayer film. Exposing the junction to a perpendicular magnetic field B , we observe a distinct Fraunhofer-like pattern in the junction critical current $I_{cJ}(B)$. Our interference pattern differs markedly from the one observed in standard junctions²¹, a consequence of the extremely weak transverse magnetic screening power of these ultrathin films: i) The periodicity of the pattern is given by the flux $\Phi_W = BW^2$ with W the junction width, a factor $W/2\lambda_L$ larger than the characteristic flux $\Phi_\lambda = 2BW\lambda_L$ in usual junctions, where λ_L denotes the London

¹Laboratory for Solid State Physics, ETH Zurich, Zurich, Switzerland. ²Research Center for Materials Nanoarchitectonics, National Institute for Materials Science, Tsukuba, Japan. ³Research Center for Electronic and Optical Materials, National Institute for Materials Science, Tsukuba, Japan. ⁴Institute for Theoretical Physics, ETH Zurich, Zurich, Switzerland. ⁵Department of Physics, Massachusetts Institute of Technology, Cambridge, Cambridge, MA, USA. ⁶Quantum Center, ETH Zurich, Zurich, Switzerland. ✉e-mail: mperego@phys.ethz.ch

penetration depth²¹. And ii), the maxima in the Fraunhofer-like pattern decay slowly $\propto 1/\sqrt{B}$, rather than the usual decay $\propto 1/B$; recognizing these differences, in the following, we refer to our experimentally observed interference pattern as a Fraunhofer pattern (FP). Interestingly, our FP exhibits pronounced jumps that we attribute to vortices penetrating/leaving the superconducting leads. Our JJ then serves as a sensor allowing for an indirect detection of vortices in gated atomically thin materials. Our observations represent the first experimental evidence for superconducting vortices in magic-angle graphene. Using a JJ allows us to detect vortices without using traditional vortex imaging techniques, which would be extremely challenging in this 2D superconductor^{22–25}. Until now, most research has focused on the microscopic origin of superconductivity in this correlated material, with a lack of vortex studies^{26–28}. Independently of the microscopic origin of superconductivity, which is still under debate, we can quantitatively analyse the observed vortex dynamics thanks to the well-developed phenomenology for these ultrathin materials^{29–34}.

Results

Setup and bulk superconductivity

We have engineered a gate-defined JJ of length $L_j = 150$ nm in a MAT4G film of width $W = 1.1$ μm along y , length $L = 6W$ along x , and thickness $d \approx 1$ nm³⁵, as illustrated in Fig. 1a, b. A graphite bottom gate (BG), a gold top gate (TG), and a gold finger gate (FG) are used to independently control the density n_1 and the displacement field D_1 in the leads and in the junction (denoted as n_j and D_j). Given the nanometer scale thickness d of the film $d \ll \lambda_L$, the device belongs to the class of weak transverse screeners, with the effective screening power given by the Pearl length $\Lambda = 2\lambda_L^2/d \gg \lambda_L$ ³⁶. With the width $W \ll \Lambda$, external magnetic fields H penetrate the entire sample and $B \approx H$.

We first analyse the bulk superconductivity observed in our MAT4G device. Fig. 1c shows the phase diagram of the film in terms of the voltage V (measured at constant probe current I in a 4-terminal configuration not crossing the JJ) as a function of n_1 and D_1 , see Fig. S3B for the same measurement taken across the JJ. Superconductivity is observed between moiré filling factors $|\nu| \approx \pm 2$ and a value slightly beyond $|\nu| \approx \pm 3$, as expected⁸, see the dark blue domes showing zero voltage. Further characterization of the superconducting domes is discussed in the Supplementary Information.

The dependence of the bulk critical current I_{cb} on the magnetic field B applied normal to the sample plane is shown in Fig. 1d for the device tuned at the green square depicted in Fig. 1c. The critical current I_{cb} is seen as a peak in the differential resistance $R = dV/dI$ which is evaluated numerically from d.c. data (transition between dark blue in Fig. 1d, zero resistance, to a finite one, light blue), where the device switches to the resistive state due to vortex motion. The field dependence of $I_{cb}(B)$ is governed by the edge- and bulk-pinning of vortices^{34,37–40}. The linear drop in $I_{cb}(B)$ at small fields is characteristic of the Bean-Livingston barrier³⁷ preventing vortices from entering the sample at the film edges $y = \pm W/2$ ^{34,39,40}, as is typical for such films. By linearly fitting I_{cb} versus B , we extract a value for the edge penetration field $B_e \approx 100$ mT, see orange dashed line in Fig. 1d. Combining this result with the zero-field critical current $I_{cb}(0) = 230$ nA and using the relation $\partial_B I_{cb}(B) = -dW^2/2\mu_0\lambda_L^2$ ³⁴, we arrive at an estimate for the London penetration depth λ_L of order 10 μm , which compares favorably with values of a few μm obtained from other estimates (here, μ_0 is the vacuum permeability). For example, we may use the bulk critical current $I_{cb}(0) \approx 230$ nA measured in Fig. 1d, obtain the critical current density $j_0 \approx 2.1 \times 10^4$ A/cm², and take this value as a lower bound for the depairing current density $j_0 = \Phi_0/3\sqrt{3}\pi\mu_0\lambda_L^2\xi$ (with $\Phi_0 = h/2e$

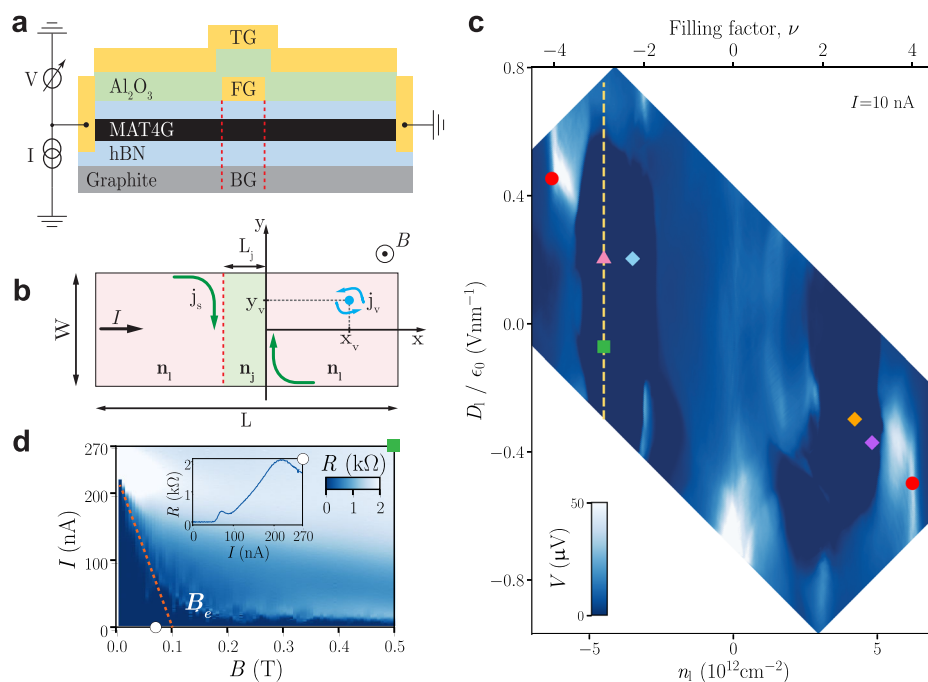


Fig. 1 | Device setup and bulk phase diagram. **a** Schematic cross-section of the thin film JJ device and measurement setup; V is the measured voltage drop and I is the applied current. The top gate (TG), finger gate (FG), and back gate (BG) are indicated. **b** Schematic top view of the film with width W (along the y -axis) and overall length L (along the x -axis); L_j is the thickness of the JJ along x . The densities in the leads and junction are denoted by n_1 and n_j , the field B and current I directions are indicated. Screening currents j_s (in green) and vortex currents j_v (light blue) circulate in opposite directions. **c** Phase diagram of the film material, with the voltage V (blue color scale) versus leads' density n_1 and displacement field D_1 ,

measured in a 4-terminal configuration not crossing the junction at a constant current $I = 10$ nA. The filling factor ν is plotted on the top axis. The blue dark regions around $|\nu| \approx 2-3$ signal superconductivity. Red dots indicate full filling where the junction is tuned into the resistive state. **d** Differential resistance R measured as a function of I and B with the device tuned to the superconducting state (green square in (c)). The orange dashed line indicates the fit to extract the edge penetration field B_e , with the inset showing a line trace recorded at the white circle $B = 72$ mT.

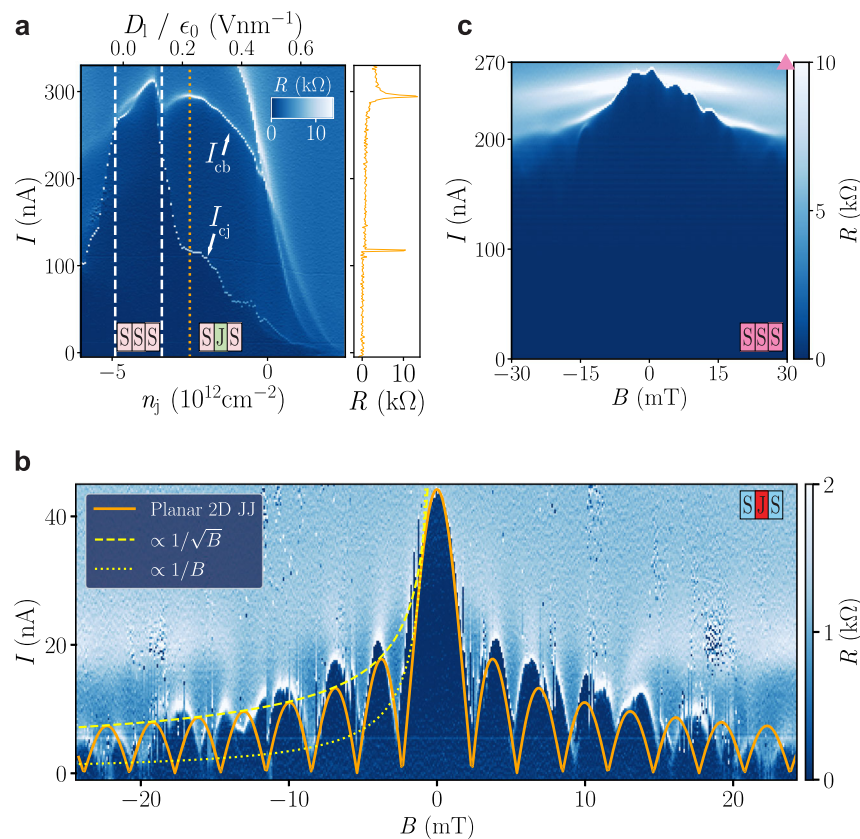


Fig. 2 | Josephson junction device and Fraunhofer pattern. **a** Differential resistance R measured as a function of I while sweeping n_j and keeping n_i fixed. D_j is fixed at zero whereas D_i is swept as shown on the top axis, following the yellow dashed line in Fig. 1c. By sweeping n_j , the junction can be tuned from a resistive to a superconducting state, resulting in a SJS or SSS configuration, with the critical currents of the bulk and junction denoted by I_{cb} and I_{cj} . A line trace of the differential resistance R is shown with n_j fixed at the dotted orange line. **b** Differential resistance R measured as a function of I and B for $n_i = -3.5 \times 10^{12}$ cm $^{-2}$, $D_j/\epsilon_0 = 0.2$ V/

nm and $n_j = -6.3 \times 10^{12}$ cm $^{-2}$, $D_j/\epsilon_0 = 0.45$ V/nm (blue-red-blue setting in Fig. 1c). The orange and yellow dashed lines show the theoretical predictions for a 2D JJ under weak screening conditions, whereas the dotted yellow line shows the rapid decay $\propto 1/B$ for a standard JJ. **c** Differential resistance R measured as a function of I and B with the entire device tuned to the pink triangle shown in the phase diagram Fig. 1c, implying that no junction is formed. This SSS configuration exhibits no interference pattern.

denoting the flux unit). Extracting a value $\xi \approx 40$ nm for the coherence length^{8,16,17} (Fig. S4), we then find an estimate $\lambda_L < 3.5 \mu\text{m}$. Finally, the low value in the saturation of I_{cb} at large fields, see Fig. 1d, is testimony of weak bulk pinning inside the film $|y| < W/2$ ²⁴, possibly due to twist-angle variation.

Josephson junction (JJ)

Keeping the leads in one of the superconducting regimes, we form a JJ in our sample by tuning the junction region into a resistive state. The formation of a JJ is confirmed by the observation of a d.c. Josephson critical current $I_{cj} < I_{cb}$, as shown in Fig. 2a, and the appearance of the Fraunhofer-like interference effect, see Fig. 2b (for details of the device fabrication and gate control see Supplementary Information Figs. S1 and S2 and Methods). The high tunability of our device allows us to define a JJ in several ways by exploring the parameter space of density n and displacement field D in the leads and the junction, see phase diagram in Fig. 1c. The formation of a JJ is achieved by tuning the junction density n_j at fixed $n_i = -4.5 \times 10^{12}$ cm $^{-2}$ and $D_j = 0$ (the displacement field D_i is bound to n_j and follows the yellow dashed line within the superconducting dome in Fig. 1c). The differential resistance R then exhibits two steps, i) at low currents I_{cj} when the junction turns resistive, and ii) at high currents I_{cb} when the leads switch to the resistive state, see orange line-trace in Fig. 2a. The two critical currents coalesce when n_j enters the superconducting state between the white dashed lines in Fig. 2a, resulting in a uniform superconducting device SSS. Away from this region, we can implement a JJ with a desired critical current I_{cj} —we refer

to this weak-link configuration as SJS, with J denoting the resistive junction region, notwithstanding its nature, metallic, semiconducting, or insulating. In all of our measurements, the junction region is tuned to the full-filling peaks ($n_j = \pm 6.2 \times 10^{12}$ cm $^{-2}$) as indicated by the red dots in Fig. 1c. This tuning is chosen to produce the most resistive state in the junction region (the junction has been tuned to a magnetically correlated state in ref. 20), see Supplementary Information and Fig. S5 and S6 for further details on junction tuning. Note that our MAT4G device admits the displacement field D_j as an additional tuning knob for changing I_{cj} as compared to junctions defined in MATBC^{9,10} (Fig. SSF).

Junction in magnetic field

A typical magnetic interference measurement with the device tuned to the junction regime is presented in Fig. 2b. The current I is swept from negative to positive values while measuring the voltage drop across the junction, all at fixed perpendicular applied field B . After each current sweep, B is stepped and a new trace is recorded. The leads are set to the superconducting state ($n_i = -3.5 \times 10^{12}$ cm $^{-2}$, $D_j/\epsilon_0 = 0.2$ V/nm, light blue rhombus in Fig. 1c) and the junction is gated to full filling ($n_j = -6.2 \times 10^{12}$ cm $^{-2}$, $D_j/\epsilon_0 = 0.45$ V/nm, red dot in Fig. 1c); we call this the blue-red-blue setting with a corresponding identifier in the top-right corner of Fig. 2b. Note that a SJS device is characterized by a pair of points in the phase diagram Fig. 1c specifying density n and displacement field D in the junction and the leads. The critical Josephson current $I_{cj}(B)$ is suppressed and modulated as B is varied, resulting in the FP shown in Fig. 2b—the observed pattern is typical for a short

junction⁴¹ and exhibits the hallmarks of a weak screening device^{30,31}. We observe field-induced oscillations of $I_{cj}(B)$ with the interference period $\Delta B \approx 3$ mT. The FP are symmetric in current and do not show any skewness. Thanks to the high tunability of our device, we can study these interference patterns throughout the phase space of both junction and leads (see Supplementary Information for further measurements with different n_i and D_j).

To further prove that the measured interference pattern is due to the JJ rather than sample inhomogeneity, we carry out the same measurement with the JJ tuned into the superconducting lobe (SSS) as shown in Fig. 2c (with $n_j = n_i \approx -4.5 \times 10^{12}$ cm⁻² and $D_j/\epsilon_0 = D_i/\epsilon_0 \approx 0.2$ V/nm, pink triangle in the phase diagram Fig. 1c). In this measurement, I_{cj} agrees with I_{cb} up to small oscillations in $I_{cj}(B)$ at low fields; their periodicity closely matches the one observed in the pattern of Fig. 2b and we attribute them to a slight mismatch in the tuning between the leads and the junction regions. No interference pattern is observed when the device is fully superconducting, compare Fig. 2b with Fig. 2c.

Fraunhofer interference pattern

Our JJ shows a Fraunhofer-type pattern $I_{cj}(B)$ that is typical for a weak screener with $\lambda \gg W$ ^{30,31,42,43}, the field B then penetrates the leads completely and the gauge-invariant phase-difference $\Delta\gamma_B(y)$ takes the form^{30,31}

$$\Delta\gamma_B(y) \approx 1.7 \frac{\Phi_W(B)}{\Phi_0} \sin(\pi y/W) \quad (1)$$

with the relevant flux determined by the junction width W only, $\Phi_W(B) = BW^2$, provided that the film leads are longer than the film width, $L \gg W$. Furthermore, the usual linear shape²¹ $\Delta\gamma_B(y) \propto y/W$ is replaced by a sine-function, $\Delta\gamma_B(y) \propto \sin(\pi y/W)$, a feature that is again due to the deep penetration of the field into the film, see Supplementary Information. This seemingly minor correction has profound consequences for the FP at large B , producing a slow decay of the maxima $\propto 1/\sqrt{B}$ in the pattern instead of the standard $1/B$ behavior.

To relate these insights to our experiment, we find $I_{cj}(B)$ by integration over the junction dimensions: assuming a sinusoidal current-phase relation $j_j(\Delta\gamma) = j_{cj} \sin(\Delta\gamma + \gamma_0)$ with γ_0 a free shift parameter, the integral over W can be evaluated exactly^{30,31} in terms of the Bessel function J_0 ,

$$\frac{I_{cj}(B)}{I_{cj}(0)} = |J_0[1.7\Phi_W(B)/\Phi_0]|, \quad (2)$$

where the choice $\gamma_0 = \pm \pi/2$ produces the largest, hence critical, current. The Bessel function J_0 then replaces the sinc-function characterizing the FP in the standard context²¹. The orange line in Fig. 2b is a fit to the data that makes use of the width $W = 1.1 \mu\text{m}$ of the film in the determination of the flux $\Phi_W(B) = BW^2$. Given that the distance between consecutive zeros of the Bessel function $J_0(s)$ is $\Delta s \approx 3.1$, we recover the periodicity $\Delta B \approx (\Delta s/1.7)\Phi_0/W^2 \approx 3$ mT. Note that the zeros in $J_0(s)$ become truly equidistant only at large values of the magnetic field. Furthermore, the maxima are well tracked by the slow decay $\propto 1/\sqrt{B}$, see the dashed yellow line at $B < 0$. The good agreement between the theoretical prediction and the experimental data holds at fields below $|B| \approx \pm 10$ mT, i.e., including the first three minima; thereafter, the fit does not work anymore due to the presence of sharp shifts in the pattern of the size of a fraction of Φ_0 . We attribute these shifts to vortices that spontaneously penetrate or leave the leads nearby the junction.

Jumps in the Fraunhofer pattern

The measured interference patterns show sudden shifts, i.e., jumps in $I_{cj}(B)$, see Figs. 2b, 3a and b. The measurement protocol for the FP described above produces maps $I_{cj}(B)$ over time scales of hours. The

sudden shifts appear in all of our junction tunings, i.e., independent of gate voltages (Fig. S11).

Pronounced jumps in I_{cj} , see black arrows in Fig. 3a, b, are observed with the leads tuned close to the center of the superconducting dome (with $n_i = 4.2 \times 10^{12}$ cm⁻², $D_i/\epsilon_0 = -0.3$ V/nm and $n_j = 6.2 \times 10^{12}$ cm⁻², $D_j/\epsilon_0 = -0.5$ V/nm, orange rhombus and red dot in the phase diagram Fig. 1c, we name it the orange-red-orange, or ‘strong-leads’ setting). They are present in both increasing and decreasing sweeps of the magnetic field, are symmetric in I , and are stable on the time scale of hours.

Vortex penetration

With these shifts present in all of our device configurations, we rule out a possible origin related to the experimental setup (Supplementary Information and Fig. S10). We rather attribute these sudden shifts to vortices penetrating and leaving the superconducting leads in the vicinity (closer than $2W$) of the junction³². Similar observations have been previously reported^{32,33,44–47}.

The presence of a vortex (at the position $\mathbf{R}_v = (x_v, y_v)$ and with a flux parallel to B , see Fig. 1b) changes the phase pattern at the junction, $\Delta\gamma(y) \rightarrow \Delta\gamma(y; \mathbf{R}_v) = \Delta\gamma_B(y) + \Delta\gamma_v(y; \mathbf{R}_v)$, adding a step-like contribution $|\Delta\gamma_v(y; \mathbf{R}_v)| < \pi$ to the phase difference, see Figs. S14–S16. The phase $|\Delta\gamma_v(y; \mathbf{R}_v)|$ as a function of y (see Supplementary Information for an explicit expression) smoothens and decreases in amplitude with increasing distance x_v of the vortex from the junction, see Figs. S14 and S15. Since the vortex currents (j_v , blue in Fig. 1b) flow opposite to the screening currents (j_s , green in Fig. 1b), the presence of a vortex *decreases* the effect of the B -field and the FP shifts to the right upon vortex entry at positive $B > 0$ (the shift is to the left for a vortex with opposite circularity entering the lead at $B < 0$). This is exactly what is seen in the experiment. For example, in Fig. 3c, d, we fit the experimental traces of Fig. 3a, b, by having 7 (in Fig. 3c) and 4 (in Fig. 3d) vortices of \pm polarity enter (upon increasing $|B|$) or leave (upon decreasing $|B|$) the device leads, see black arrows.

The magnitude of the shift in the FP is primarily determined by the distance x_v between the vortex and the junction (see Figs. S14 and S15). When changing the y_v coordinate, the largest FP-shifts occur when a vortex is at the center of the film $y_v = 0$, and their magnitude decreases as the vortex approaches the edges $y_v = \pm W/2$, see Fig. S16. Additionally, the y_v coordinate modifies the minima in the FP—the sharp minima with $I = 0$ become rounded at intermediate values $0 < y_v < W/2$, see Fig. S16. In our fit, we place the vortices at the center of the film, i.e., $y_v = 0$, and tune the pattern’s shifts by choosing vortex positions in the range $0.3 < |x_v|/W < 0.8$ (\rightarrow smallshifts), see Fig. 1b (detailed parameters are cited in the Supplementary Information). The resolution of the FP minima in the experiment is not sufficient to determine a precise value for the y_v coordinate. Note that in Figs. 3a and b, vortices have left the device at $B = 0$ in both cases. Both the local change in the FP at individual jumps and the accumulated shift at larger magnetic fields are well reproduced by the fit. When the field amplitude $|B|$ exceeds 10 mT, the patterns become blurred, and the observation of individual jumps is hampered; however, the JJ is still sensitive to the presence of vortices.

Vortex fluctuations

We close our discussion with the analysis of another data set with the leads tuned away from the center of the superconducting dome at a ‘weak-leads’ setting ($n_i = 4.8 \times 10^{12}$ cm⁻², $D_i/\epsilon_0 = -0.3$ V/nm and $n_j = 6.2 \times 10^{12}$ cm⁻², $D_j/\epsilon_0 = -0.5$ V/nm, see the purple rhombus and red dot in the phase diagram Fig. 1c, or ‘weak-leads’ setting). This choice of parameters reduces the superfluid density ρ_s of the leads²⁶ and at the same time the vortex energy $\epsilon_0 d = \pi\rho_s$, where $\epsilon_0 = (4\pi/\mu_0)(\Phi_0/4\pi\lambda_L)^2$ is the vortex line energy. The latter determines the edge barrier U_e for vortex penetration, with U_e smaller than $2\epsilon_0 d$ and decreasing with increasing field B , as follows from the analysis in ref. 29, see Fig. S17A in

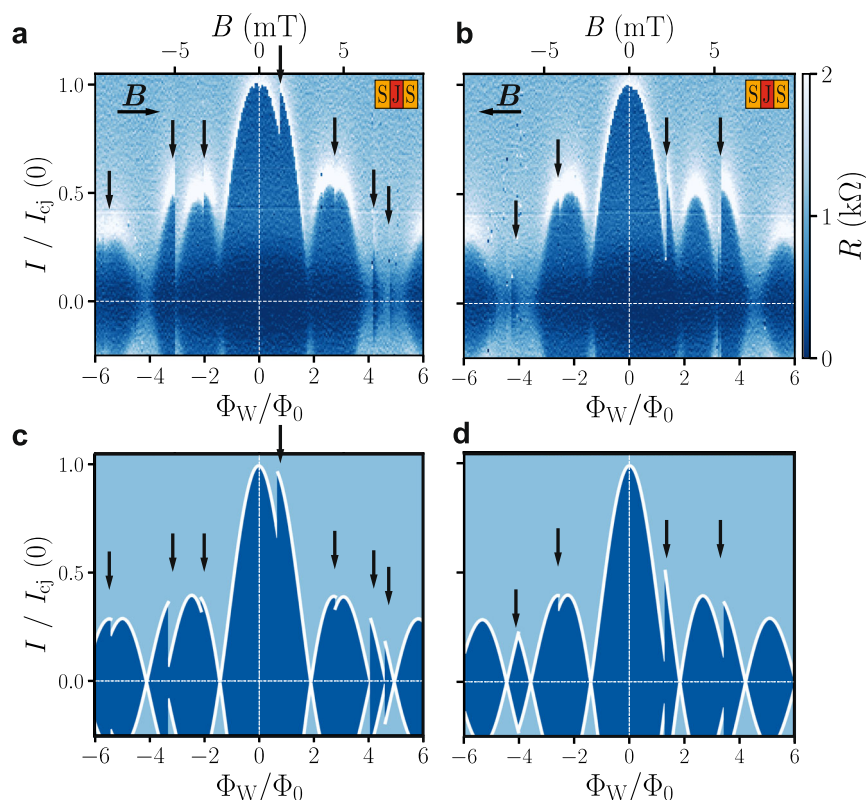


Fig. 3 | Vortex penetration. Differential resistance R measured as a function of I and B , for a forward magnetic-field sweep in (a) and a backward sweep in (b). The bottom axes show the corresponding scaled flux Φ_W/Φ_0 penetrating junction and leads, where $\Phi_W = BW^2$. The tuning parameters are $n_1 = 4.2 \times 10^{12} \text{ cm}^{-2}$, $D/\epsilon_0 = -0.3 \text{ V}$

nm and $n_2 = 6.2 \times 10^{12} \text{ cm}^{-2}$, $D/\epsilon_0 = -0.5 \text{ V/nm}$ ('strong-leads' setting). Sudden shifts of the interference pattern are highlighted with black arrows. Theoretical fits of the measured Fraunhofer patterns (a) and (b) on the basis of the analysis in Ref. 32, with 7 (in (c)) and 4 (in (d)) vortices leaving/penetrating the leads.

the Supplementary Information. Combining the reduced edge barrier U_e with an increased temperature T , we observe a boost in vortex dynamics, i.e., enhanced vortex fluctuations. Indeed, the FP in Fig. 4a, measured at $T = 100 \text{ mK}$, exhibits pronounced bi-stability effects in the voltage-current characteristic, see the grainy white-dark-blue features in Fig. 4a around $B \approx 1.5 \text{ mT}$ and $B \approx 2.7 \text{ mT}$. We associate these with vortices penetrating and leaving the leads, thereby shifting the FP back and forth and switching between two different $V(I)$ curves. Furthermore, at these elevated temperatures, the $V-I$ characteristic of the junction is rounded, with the sharp onset of dissipation at I_{c_j} replaced by a smooth non-linear rise; we attribute this rounding in $V(I)$ to phase-slips within the Josephson junction^{48,49}. Figure 4b shows both of these effects, phase-slips smoothing the dissipative crossover and sharp steps due to vortex dynamics at $B \equiv B^* = 2 \text{ mT}$, see black arrows in Fig. 4a. The sharp steps in the $V-I$ curve at $B^* = 2 \text{ mT}$ manifest as white-dark-blue pairs of dots in the differential resistance plot of Fig. 4a.

Next, we fix the field $B^* = 2 \text{ mT}$ and the bias current $I^* = 4 \text{ nA}$ (black dashed line in Fig. 4b), at a point where the presence (absence) of a vortex causes changes in the $V(I)$ characteristic, and measure the voltage as a function of time. A typical time-trace exhibiting telegraph-type voltage-noise is shown in Fig. 4c. The timescale t of these fluctuations is of order seconds and decreases rapidly with temperature, see Fig. 4d, as typical for a thermally activated process (see Supplementary Information, Fig. S8, for the counting statistics of these fluctuations). Below 90 mK , the activation process loses its temperature dependence, which we may attribute to a changeover to a quantum tunneling process of vortices⁵⁰.

Assuming thermal activation of vortices over the edge barrier governs the voltage fluctuations, we can derive an energy scale for the vortex energy $\epsilon_0 d$ and hence for the superfluid density $\rho_s = \epsilon_0 d/\pi$.

Given a barrier U_e at temperature T and an attempt time t_0 , a vortex requires a time $t \sim t_0 \exp[U_e/T]$ to overcome the barrier and penetrate into the film leads (we set k_B to unity). Knowing the typical dynamical time t of vortex fluctuations, we can derive a quite accurate estimate for $U_e \approx T \ln(t/t_0)$. Making use of a typical attempt time^{51,52} $t_0 \sim 10^{-11} \text{ s}$, a typical dwell time $t \sim 1 \text{ s}$ as observed in our experiment Fig. 4c, and the temperature $T = 100 \text{ mK}$, we find a barrier $U_e \approx 2.5 \text{ K}$. The barrier U_e remains constant upon increasing the temperature to $T = 115 \text{ mK}$, as supported by the observed decrease in dwell time t . This is illustrated in Fig. 4d, where the black dashed line shows the expected exponential decay of t . From this result, and using the relation $U_e \approx \epsilon_0 d$, see Fig. S17A, we can extract a value $\rho_s \approx 0.8 \text{ K}$ for the superfluid density and a London penetration depth $\lambda_L \sim 2.8 \mu\text{m}$. Furthermore, using the relation $T_{\text{BKT}} = \epsilon_0(T_{\text{BKT}})d/2$ and ignoring the reduction in $\epsilon_0(T)$ at higher temperatures, we find an upper limit for the Berezinskii-Kosterlitz-Thouless transition temperature $T_{\text{BKT}} < 1.2 \text{ K}$.

Recently, the superfluid density ρ_s of twisted-layer graphene has been determined using kinetic inductance measurements, both for a trilayer film²⁶ and for a bilayer system²⁷. Given the differences in the various systems, the comparison of the results in refs. 26,27 with our findings has to remain on a qualitative level, also owing to the fact that our analysis is done away from the superconducting dome center where ρ_s is well defined. While for the trilayer film a value ρ_s between 0.1 K and 0.45 K has been reported, a value up to $\sim 1.2 \text{ K}$ has been measured for the bilayer system. Our value $\rho_s \approx 0.8 \text{ K}$ then is well within this range.

Discussion

In conclusion, we have demonstrated the formation of a gate-defined Josephson junction in MAT4G and its application as a vortex sensor. The measured interference patterns agree excellently with the

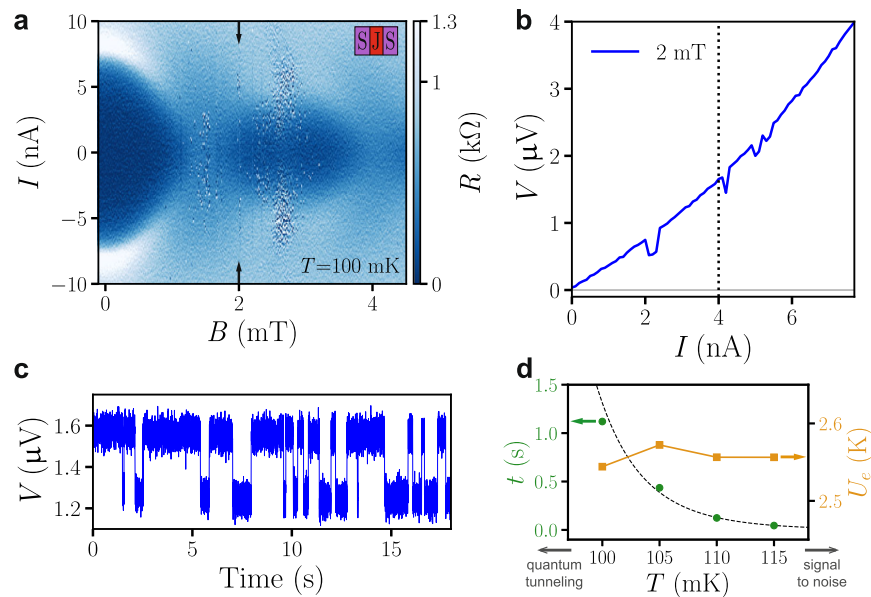


Fig. 4 | Vortex fluctuations. **a** Differential resistance R measured at $T = 100$ mK as a function of I and B with parameters $n_1 = 4.8 \times 10^{12} \text{ cm}^{-2}$, $D_j/\epsilon_0 = -0.3 \text{ V/nm}$ and $n_2 = 6.2 \times 10^{12} \text{ cm}^{-2}$, $D_j/\epsilon_0 = -0.5 \text{ V/nm}$ ('weak-leads' setting). The Fraunhofer pattern is smoothed and white–dark-blue speckles mark the presence of bistabilities in the V – I characteristic. **b** Voltage–current trace at $B^* = 2.0$ mT, see arrows in Fig. 4a. The V – I characteristic is rounded and exhibits pronounced steps; we associate the rounding with the presence of phase slips in the junction and the steps with vortex fluctuations in the leads. The steps manifest in the speckles visible in Fig. 4a. **c** Time

trace of the voltage V measured at fixed $B^* = 2.0$ mT and current $I^* = 4$ nA, see dotted line in Fig. 4b. We associate the telegraph-type noise with vortex fluctuations in the leads. **(d)** In green, vortex fluctuations timescale t versus temperature T extracted from the statistical analysis (Fig. S8) of the telegraph-type noise in Fig. 4c. The measured time scales decay in temperature from $t \sim 1.2$ s to $t \sim 0.04$ s. The expected theoretical decay of t is plotted with the black dashed line. The corresponding barrier $U_e = T \ln(t/t_0) \approx 2.56$ K is shown in orange and is seen to remain constant as expected for an activated process.

predicted behavior for a weak transverse screener with a Pearl length surpassing the sample dimension, $\Lambda > W$. Our data enable us to precisely track the entry and exit of vortices from the device leads and find their location away from the junction. Our observation of vortices in MAT4G using a Josephson junction sensor opens new avenues for exploring vortex motion in this new class of twisted materials.

Methods

Fabrication details

We fabricated a MAT4G stack using the dry pick-up method⁵³. Graphene and hexagonal boron nitride (hBN) flakes were exfoliated on a 285 nm p : Si/SiO₂ wafer. A graphene flake of around 90 μm by 20 μm was scratched into four pieces using a tungsten needle with a tip diameter of 2 μm controlled by a micromanipulator. We then picked up each flake using a polydimethylsiloxane/polycarbonate stamp. The top hBN flake, with a thickness of 25 nm, was picked up at 110 °C. Afterwards, the four graphene flakes were picked up at 40 °C while alternatively rotating the stage by $\pm 1.8^\circ$. To pick up the bottom hBN flake, with a thickness of 62 nm, the flake was contacted by the stack at 40 °C and the temperature of the stage was raised to 95 °C. The stack was then finished by picking up a graphite flake of thickness 23 nm at 100 °C. Afterwards, the stack was deposited on a p : Si/SiO₂ chip at 170 °C. The polycarbonate stamp was cleaned using dichloromethane.

To contact the MAT4G, we fabricated edge contacts⁵⁴ made by electron beam lithography and reactive ion etching. We etched using CHF₃/O₂ (40/4 sccm, 60W) and evaporated Cr/Au (10/70 nm). The finger gate and the electrode lines were then defined by depositing Cr/Au (10/80 nm). Next, the mesa was defined by etching using CHF₃/O₂ (40/4 sccm, 60W). Afterwards, a layer of 30 nm of aluminum oxide was deposited by atomic layer deposition. The top gate and its electrode line were then fabricated using electron beam lithography and evaporating Cr/Au (10/80 nm). Optical images after each fabrication step are shown in Figs. S1, A–D.

Measurement setup

We carry out all the measurements in a dilution refrigerator that uses a mixture of ³He and ⁴He with a base temperature of 55 mK (unless stated otherwise). Our measurements are current-biased, i.e., we apply a current and measure the voltage drop in two (2T), three (3T), and four-terminal (4T) setups, see Figs. S1E–G. In the two and three-terminal configuration, we correct for contact resistances. To generate the bias current, we use a home-built d.c. source in series with a 10 M Ω or 100 M Ω resistor. The voltage is amplified using a d.c. amplifier built-in-house (see ref. 55) and its output is measured with a Hewlett-Packard 3441A digital multimeter. The bottom, top, and finger gates are connected to d.c. voltage sources also built in-house. When performing radio-frequency measurements, the top gate is connected to a Rhode and Schwarz SMB 100 A signal generator using a bias-tee with $R = 10 \text{ k}\Omega$ and $C = 100 \text{ nF}$. For the statistical analysis of vortex fluctuations, the output voltage is further amplified with a gain amplifier, low-pass filtered at 1.1 kHz, and recorded in time using a National Instruments BNC-2110 data acquisition card (DAQ) with a sampling frequency of 20 kHz.

Data availability

The data supporting the findings of this study, together with the code for plotting the figures, is available online through the ETH Research Collection at <https://doi.org/10.3929/ethz-b-000742291>.

References

1. Cao, Y. et al. Correlated insulator behaviour at half-filling in magic-angle graphene superlattices. *Nature* **556**, 80–84 (2018).
2. Yankowitz, M. et al. Tuning superconductivity in twisted bilayer graphene. *Science* **363**, 1059–1064 (2019).
3. Lu, X. et al. Superconductors, orbital magnets and correlated states in magic-angle bilayer graphene. *Nature* **574**, 653–657 (2019).
4. Cao, Y. et al. Unconventional superconductivity in magic-angle graphene superlattices. *Nature* **556**, 43–50 (2018).

5. Park, J. M. et al. Tunable strongly coupled superconductivity in magic-angle twisted trilayer graphene. *Nature* **590**, 249–255 (2021).
6. Hao, Z. et al. Electric field-tunable superconductivity in alternating-twist magic-angle trilayer graphene. *Science* **371**, 1133–1138 (2021).
7. Carr, S. et al. Twistronics: Manipulating the electronic properties of two-dimensional layered structures through their twist angle. *Phys. Rev. B* **95**, 075420 (2017).
8. Park, J. M. et al. Robust superconductivity in magic-angle multilayer graphene family. *Nat. Mater.* **21**, 877–883 (2022).
9. Rodan-Legrain, D. et al. Highly tunable junctions and non-local Josephson effect in magic-angle graphene tunnelling devices. *Nat. Nanotechnol.* **16**, 769–775 (2021).
10. Vries, F. K. et al. Gate-defined Josephson junctions in magic-angle twisted bilayer graphene. *Nat. Nanotechnol.* **16**, 760–763 (2021).
11. Díez-Mérida, J. et al. Symmetry-broken Josephson junctions and superconducting diodes in magic-angle twisted bilayer graphene. *Nat. Commun.* **14**, 2396 (2023).
12. Portolés, E. et al. A tunable monolithic SQUID in twisted bilayer graphene. *Nat. Nanotechnol.* **17**, 1159–1164 (2022).
13. Díez-Carlon, A. et al. Probing the flat-band limit of the superconducting proximity effect in twisted bilayer graphene Josephson junctions. arXiv preprint arXiv:2502.04785 (2025).
14. Rothstein, A. et al. Gate-defined single-electron transistors in twisted bilayer graphene. *Nano Lett.* **25**, 6429–6437 (2025).
15. Kim, H. et al. Evidence for unconventional superconductivity in twisted trilayer graphene. *Nature* **606**, 494–500 (2022).
16. Zhang, Y. et al. Promotion of superconductivity in magic-angle graphene multilayers. *Science* **377**, 1538–1543 (2022).
17. Burg, G. W. et al. Emergence of correlations in alternating twist quadrilayer graphene. *Nat. Mater.* **21**, 884–889 (2022).
18. Mukherjee, A. et al. Superconducting magic-angle twisted trilayer graphene with competing magnetic order and moiré inhomogeneities. *Nat. Mater.*, 1–7 (2025).
19. Khalaf, E. et al. Magic angle hierarchy in twisted graphene multilayers. *Phys. Rev. B* **100**, 085109 (2019).
20. Ronen, Y. et al. Competing Orbital Magnetism and Superconductivity in Electrostatically Defined Josephson Junctions of Alternating Twisted Trilayer Graphene. Unpublished (2025).
21. Tinkham, M. Introduction to Superconductivity. Dover Publications, Mineola, NY (2004).
22. Essmann, U. & Träuble, H. The direct observation of individual flux lines in type II superconductors. *Phys. Lett. A* **24**, 526 (1967).
23. Hess, H. et al. Scanning-tunneling-microscope observation of the Abrikosov flux lattice and the density of states near and inside a fluxoid. *Phys. Rev. Lett.* **62**, 214 (1989).
24. Bending, J. N. Local magnetic probes of superconductors. *Adv. Phys.* **48**, 449 (1999).
25. Embon, L. et al. Probing dynamics and pinning of single vortices in superconductors at nanometer scales. *Sci. Rep.* **5**, 7598 (2015).
26. Banerjee, A. et al. Superfluid stiffness of twisted trilayer graphene superconductors. *Nature* **638**, 93–98 (2025).
27. Tanaka, M. et al. Superfluid stiffness of magic-angle twisted bilayer graphene. *Nature* **638**, 99–105 (2025).
28. Portolés, E. et al. Quasiparticle and superfluid dynamics in Magic-Angle Graphene. *Nat. Commun.* **16**, 1–9 (2025).
29. Stejic, G. et al. Effect of geometry on the critical currents of thin films. *Phys. Rev. B* **49**, 1274–1288 (1994).
30. Moshe, M. et al. Edge-type Josephson junctions in narrow thin-film strips. *Phys. Rev. B* **78**, 020510 (2008).
31. Clem, J. R. Josephson junctions in thin and narrow rectangular superconducting strips. *Phys. Rev. B* **81**, 144515 (2010).
32. Kogan, V. G. & Mints, R. G. Interaction of Josephson junction and distant vortex in narrow thin-film superconducting strips. *Phys. Rev. B* **89**, 014516 (2014).
33. Kogan, V. G. & Mints, R. G. Manipulating Josephson junctions in thin-films by nearby vortices. *Phys. C* **502**, 58 (2014).
34. Gaggioli, F. et al. Superconductivity in atomically thin films: two-dimensional critical state model. *Phys. Rev. Res.* **6**, 023190 (2024).
35. Rickhaus, P. et al. The electronic thickness of graphene. *Sci. Adv.* **6**, 8409 (2020).
36. Pearl, J. Current distribution in superconducting films carrying quantized fluxoids. *Appl. Phys. Lett.* **5**, 65–66 (1964).
37. Bean, C. P. & Livingston, J. D. Surface Barrier in Type-II Superconductors. *Phys. Rev. Lett.* **12**, 14–16 (1964).
38. Larkin, A. & Ovchinnikov, Y. N. Pinning in type II superconductors. *J. Low. Temp. Phys.* **34**, 409–428 (1979).
39. Maksimova, G. M. Mixed state and critical current in narrow semi-conducting films. *Fiz. Tverd. Tela* **40**, 1773 (1998).
40. Plourde, B. et al. Influence of edge barriers on vortex dynamics in thin weak-pinning superconducting strips. *Phys. Rev. B* **64**, 014503 (2001).
41. Barone, A. et al. Physics and applications of the Josephson effect. John Wiley & Sons, Ltd, New York (1982).
42. Rosenthal, P. A. et al. Flux focusing effects in planar thin-film grain-boundary Josephson junctions. *Appl. Phys. Lett.* **59**, 3482 (1991).
43. Humphreys, R. G. & Edwards, J. A. YBa₂Cu₃O₇ thin film grain boundary junctions in a perpendicular magnetic field. *Phys. C* **210**, 42 (1993).
44. Hyun, O. B. et al. Elementary pinning Force for a Superconducting Vortex. *Phys. Rev. Lett.* **58**, 599 (1987).
45. Hyun, O. B. et al. Motion of a single superconducting vortex. *Phys. Rev. B* **40**, 175 (1989).
46. Mitchell, E. E. et al. Vortex penetration and hysteretic behaviour of narrow planar Josephson junctions in a magnetic field. *Phys. C* **321**, 219 (1999).
47. Golod, T. et al. Detection of the phase shift from a single Abrikosov vortex. *Phys. Rev. Lett.* **104**, 227003 (2010).
48. Ivanchenko, Y. M. & Zil'berman, L. A. Destruction of Josephson current by fluctuations. *JETP Lett. (USSR)* **8**, 113 (1968).
49. Ambegaokar, V. & Halperin, B. I. Voltage due to thermal noise in the dc Josephson Effect. *Phys. Rev. Lett.* **22**, 1364 (1969).
50. Blatter, G., Feigel'man, M. V., Geshkenbein, V. B., Larkin, A. I. & Vinokur, V. M. Vortices in high-temperature superconductors. *Rev. Mod. Phys.* **66**, 1125–1388 (1994).
51. Malozemoff, A. P. & Fisher, M. P. A. Universality in the current decay and flux creep of Y-Ba-Cu-O high-temperature superconductors. *Phys. Rev. B* **42**, 6784–6786 (1990).
52. Kopylov, V. N. et al. The role of surface effects in magnetization of high-T_c superconductors. *Phys. C* **170**, 291 (1990).
53. Kim, K. et al. van der Waals heterostructures with high accuracy rotational alignment. *Nano Lett.* **16**, 1989–1995 (2016).
54. Wang, L. et al. One-dimensional electrical contact to a two-dimensional material. *Science* **342**, 614–617 (2013).
55. Märki, P., Braem, B.A. & Ihn, T. Temperature-stabilized differential amplifier for low-noise DC measurements. *Rev. Sci. Instrum.* **88** (2017).

Acknowledgements

We thank Peter Märki and the staff of the ETH cleanroom facility FIRST for technical support. We acknowledge fruitful discussions with Vladimir Kogan and Manfred Sigrist. We thank Giulia Zheng for her support during the project. Financial support was provided by the European Graphene Flagship Core3 Project, H2020 European Research Council (ERC) Synergy Grant under Grant Agreement 951541, the European Union's Horizon 2020 research and innovation program under grant agreement number 862660/QUANTUM E LEAPS, the European Innovation Council under grant agreement number 101046231/FantastiCOF, the EU Cost

Action CA21144 (SUPERQUMAP), and NCCR QSIT (Swiss National Science Foundation, grant number 51NF40-185902). K.W. and T.T. acknowledge support from the JSPS KAKENHI (Grant numbers 21H05233 and 23H02052) and the World Premier International Research Center Initiative (WPI), MEXT, Japan. F.G. is grateful for the financial support from the Swiss National Science Foundation (Postdoc.Mobility Grant no. 222230).

Author contributions

M.P. fabricated the device. T.T. and K.W. supplied the hBN crystals. M.P. and C.G.A. performed the measurements. M.P. and C.G.A. analyzed the data. F.G., V.G. and G.B. developed the theoretical model. M.P. and G.B. wrote the manuscript, and all authors were involved in the reviewing process. M.P., C.G.A., E.P., A.M.T. and A.O.D. discussed the data. M.P., E.P., K.E. and T.I. conceived and designed the experiment. T.I. and K.E. supervised the work.

Competing interests

The authors declare no competing interests.

Additional information

Supplementary information The online version contains supplementary material available at <https://doi.org/10.1038/s41467-025-65123-1>.

Correspondence and requests for materials should be addressed to Marta Perego.

Peer review information *Nature Communications* thanks the anonymous reviewers for their contribution to the peer review of this work. A peer review file is available.

Reprints and permissions information is available at <http://www.nature.com/reprints>

Publisher's note Springer Nature remains neutral with regard to jurisdictional claims in published maps and institutional affiliations.

Open Access This article is licensed under a Creative Commons Attribution-NonCommercial-NoDerivatives 4.0 International License, which permits any non-commercial use, sharing, distribution and reproduction in any medium or format, as long as you give appropriate credit to the original author(s) and the source, provide a link to the Creative Commons licence, and indicate if you modified the licensed material. You do not have permission under this licence to share adapted material derived from this article or parts of it. The images or other third party material in this article are included in the article's Creative Commons licence, unless indicated otherwise in a credit line to the material. If material is not included in the article's Creative Commons licence and your intended use is not permitted by statutory regulation or exceeds the permitted use, you will need to obtain permission directly from the copyright holder. To view a copy of this licence, visit <http://creativecommons.org/licenses/by-nc-nd/4.0/>.

© The Author(s) 2025